processes

MDPI

Article

The Impact of Formation Anisotropy and Stresses on Fractural Geometry—A Case Study in Jafurah's Tuwaiq Mountain Formation (TMF), Saudi Arabia

Ali Shawaf, Vamegh Rasouli * and Abdesselem Dehdouh

Energy and Petroleum Engineering Department, University of Wyoming, Laramie, WY 82071, USA; aalshawa@uwyo.edu (A.S.); adehdouh@uwyo.edu (A.D.)
* Correspondence: vrasouli@uwyo.edu

Abstract: Multi-stage hydraulic fracturing (MsHF) is the main technology to improve hydrocarbon recovery from shale plays. Associated with their rich organic contents and laminated depositional environments, shales exhibit transverse isotropic (TI) characteristics. In several cases, the lamination planes are horizontal in shale formations with a symmetric axis that are vertical to the bedding plane; hence, shale formations are known as transverse isotropic vertical (TIV) rocks. Ignoring the TIV nature of shale formations leads to erroneous estimates of in situ stresses and consequently to inefficient designs of fractural geometry, which negatively affects the ultimate recovery. The goal of this study is to investigate the effects of TIV medium characteristics on fractural geometry, spacing, and stress shadow development in the Jurassic Tuwaiq Mountain formation (TMF) in the Jafurah basin, which is a potential unconventional world-class play. This formation is the main source for prolific Jurassic oil reservoirs in Saudi Arabia. On the basis of a petrophysical evaluation in the Jafurah basin, TMF exhibited exceptional unconventional gas characteristics, such as high total organic content (TOC) and low clay content, and it was in the proper maturity window for oil and gas generation. The unconventional Jafurah field covers a large area that is comparable to the size of the Eagle Ford shale play in South Texas, and it is planned for development through multi-stage hydraulic fracturing technology. In this study, analytical modeling was performed to estimate the fractural geometry and in situ stresses in the anisotropic medium. The results show that the Young's modulus anisotropy had a noticeable impact on fractural width, whereas the impact of Poisson's ratio was minimal. Moreover, we investigated the impact of stress anisotropy and other rock properties on the stress shadow, and found that a large stress anisotropy could result in fractures being positioned close to one another or theoretically without minimal fractural spacing concerns. Additionally, we estimated the fractural aspect ratio in different propagation regimes and observed that the highest aspect ratio had occurred in the fractural toughness-dominated regime. This study also compares the elastic properties and confirms that TMF exhibited greater anisotropic properties than those of Eagle Ford. These findings have practical implications for field operations, particularly with regard to the fractural geometry and proppant placement.

Keywords: elastic properties; hydraulic fracturing; elastic anisotropy

check for updates

Citation: Shawaf, A.; Rasouli, V.; Dehdouh, A. The Impact of Formation Anisotropy and Stresses on Fractural Geometry—A Case Study in Jafurah's Tuwaiq Mountain Formation (TMF), Saudi Arabia. *Processes* **2023**, *11*, 1545. https://doi.org/10.3390/pr11051545

Academic Editor: Qingbang Meng

Received: 24 April 2023
Revised: 9 May 2023
Accepted: 11 May 2023
Published: 18 May 2023

1. Introduction

Growing global demands for energy associated with the depletion of conventional hydrocarbon reservoirs have shifted the industry to the rapid development of unconventional resources, namely, geological oil and gas formations that are characterized by low porosity, ultra-low reservoir permeability, poor pore-scale connectivity, and high total organic content [1,2]. The permeability of unconventional formations is usually less than 0.1 mD (in the range of micro to nano Darcy), and hydraulic fracturing (HF) stimulation is required to economically produce hydrocarbons from these resources [3,4]. Hydraulic fracturing involves the injection of fluids into a wellbore at high pressure, which creates fractures in the rock formation. These fractures help in improving fluid flow by increasing permeability, allowing for greater production rates [5,6]. Additionally, proppants are used to keep the fractures open, maintaining enhanced permeability and optimizing production [7]. Several studies using numerical simulations were conducted to evaluate the performance of hydraulic fracturing [8]. These simulations enable the analysis of various parameters and factors that could affect the efficiency of the process [9], such as the injection rate, fluid viscosity, rock properties, and proppant characteristics [10]. Examples of unconventional resources include shale gas and oil, tight sands, coal bed methane, and heavy oil and gas hydrates [11].

Hydraulic fracturing alters the magnitude and orientation of an in situ stress field in the neighborhood of the fracture. There are three orthogonal principal stresses, namely, vertical stress (σ_v), maximal horizontal stress (σ_H), and minimal horizontal stress (σ_h) [12,13]. Ideally, a hydraulic fracture (HF) preferentially propagates perpendicular to the minimal principal stress. The stress perturbation resulting from the opening of propped fractures is known as the stress shadow, which considerably affects the geometry and propagation of the subsequent fractures, hindering the well's productivity. The impact of stress shadows and the resulting stress anisotropic changes can be minimized by optimizing the fractural spacing [14,15]

Most of the developed geomechanical modes to study the effect of the stress shadow are based on the assumption of isotropic formation properties. This means that rock properties can be defined using the two elastic properties of Young's modulus and Poisson's ratio. However, in most cases, including the case study of this research, shale formations are transverse isotropic (TI) in which the rock properties are similar in the horizontal plane, but different in the vertical direction, perpendicular to the bedding [16,17]. As most shale formations are nearly horizontal with a symmetric vertical axis, these types of formations are referred to as a vertical TI medium (TIV). For TIV formations, three samples should be taken in the perpendicular and parallel directions, and at 45 degrees with respect to the bedding in order to obtain the five elastic properties of such rocks. These elastic properties are two Young's moduli, one perpendicular and one parallel to the bedding (E_v, E_h), two Poisson's ratios, one perpendicular and one parallel to the bedding (v_v, v_h), and one shear modulus (G_{vh}), [18].

The anisotropy of mechanical properties should be considered for completion and hydraulic-fracture design [18,19]. Simplifying the anisotropic characteristics of shales to isotropic conditions has resulted in large errors in the estimation of hydraulic fractural design parameters and led to inappropriate conclusions and poor production strategies [19–21]. Therefore, it is necessary to apply TIV formulations to simulations of shale formations and HF designs.

Several studies have suggested that elastic anisotropy plays an important role in controlling the geometry and spacing of hydraulic fractures in shale formations. The authors in found that the elastic anisotropy influenced the orientation of hydraulic fractures and the spacing between them. When the elastic anisotropy ratio (i.e., the ratio of Young's modulus in the horizontal direction to that in the vertical direction) was low, the fractures tended to propagate in a perpendicular direction to the minimal stress direction. On the other hand, when the elastic anisotropy ratio was high, the fractures tended to propagate in a parallel direction to the minimal stress direction. Recently, the authors in [22] investigated the role of elastic anisotropy in controlling the hydraulic fractural geometry in shale reservoirs using a numerical modeling approach. When the elastic anisotropy ratio was high, the hydraulic fractures tended to propagate along the planes of the maximal horizontal stress, resulting in long and planar fractures. On the other hand, when the elastic anisotropy ratio was low, the hydraulic fractures tended to be more complex and irregular in shape, with multiple branches and nonplanar geometries.

As presented in the above examples, shale formations are inherently anisotropic in which elastic mechanical properties vary with the direction. This anisotropic behavior of mechanical properties impacts the estimation of local in situ stress, fractural geometry, and stress-shadow development in shale formations. Hence, the complete characterization of anisotropic geomechanical properties is essential for the successful development of shale formations. The goal of this study is to investigate the effects of TIV medium characteristics on fractural spacing, geometry, and stress-shadow development. Theory-based TIV analytical modeling was performed to estimate the fractural geometry and in situ stresses in an anisotropic medium using data from the Jafurah shale play.

2. Source of Data

The liquid-rich Jafurah shale play is located east of the greater Ghawar field, which is the world's largest conventional oil field located in the eastern region of Saudi Arabia (see Figure 1) [23,24]. On the basis of exploration and appraisal programs, the ultimate recovery of natural gas and liquids from the play is estimated to be around 200 trillion cubic ft equivalent (tcfe), and the first commercial production is to start in 2025 [25,26]. On the basis of a petrophysical evaluation in the Jafurah basin, the primary target formation is the Jurassic Tuwaiq Mountain (TMF), which is the principal rock source of the prolific Arab-D carbonate reservoir [25,26]. TMF exhibits exceptional unconventional gas characteristics, such as a high total organic content (TOC) and low clay content, and it is in the proper maturity window for oil and gas generation. The thickness of the TMF interval ranges from 110 to 150 ft across the Jafurah basin [23–25].

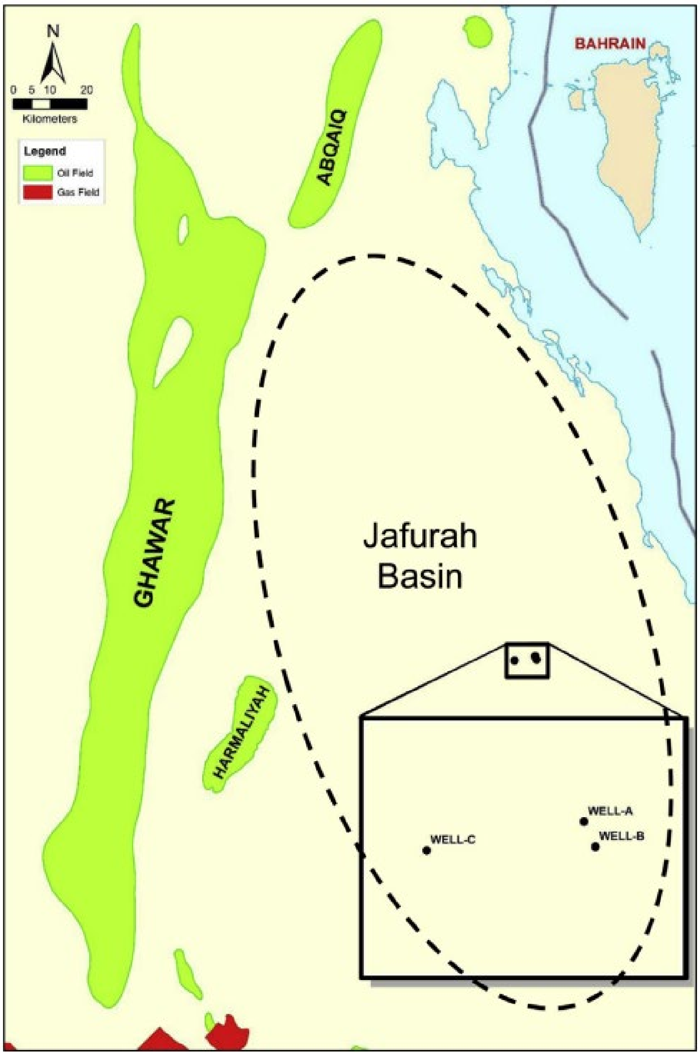

Figure 1. Location map of the estimated outline of Jafurah basin (dashed white line), which is located to the east of the gigantic Ghawar prolific oil field in Saudi Arabia [27].

2.1. Geological Setting

Throughout the Mesozoic period, the northeastern passive margin of the Afro-Arabian plate evolved into an extensive continental shelf. During the Jurassic period, deposition in the Arabian Gulf region was mainly dominated by platform carbonates. Local structuring within the shelf associated with differential subsidence resulted in the formation of intra-shelf basins. These intra-shelf basins formed within the interior of an extensive shallow-water carbonate platform that had been separated from the open ocean by a high energy platform margin [24,27].

The Jurassic successions of the Arabian plate mainly consist of marine carbonates deposited on the Arabian carbonate platform. The targeted Jurassic source rocks are calcareous and interpreted as having been deposited in a restricted marine environment within these intra-shelf basins. Organic-rich sediments were deposited into a starved shallow intra-shelf basin at the distal end of a broad carbonate ramp. It is composed of cycles of laminated organic-rich lime–mud wackestones. Figure 2 presents a generalized geological setting of the Middle and Upper Jurassic stratigraphy in Jafurah basin [24,27].

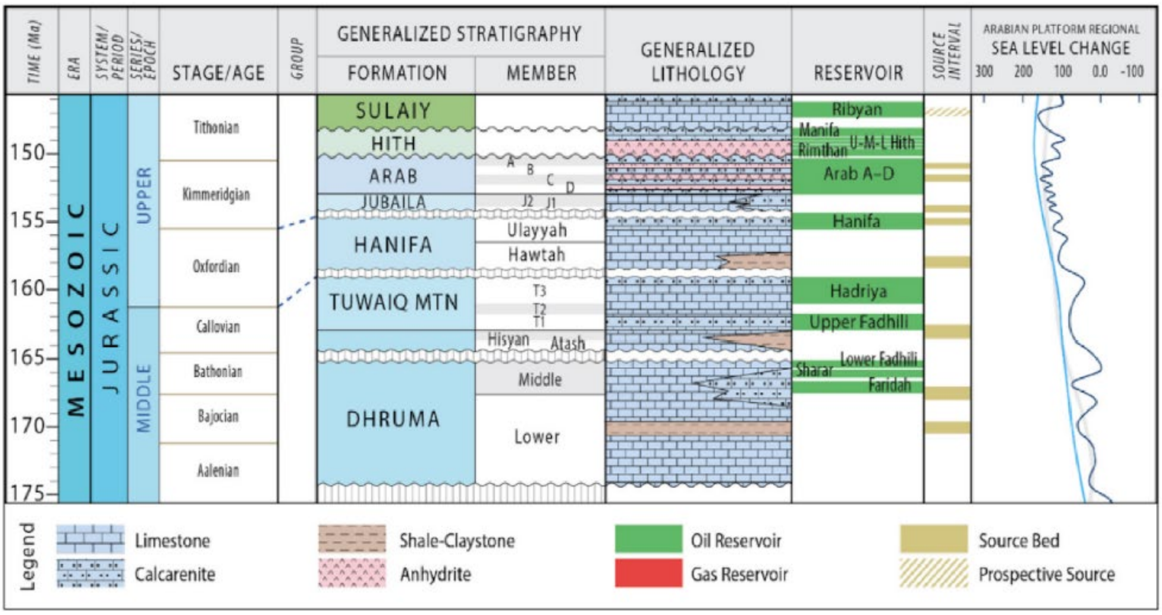

Figure 2. Generalized geological column of the Jurassic period in Jafurah basin, including the Tuwaiq Mountain formation [27].

2.2. Petrophysical Evaluation

Wireline logs were acquired from several vertical pilot wells in Jafurah basin that included calipers, sonic, density, neutron porosity, and spectral gamma ray logs [28]. Figure 3 illustrates a representative calibrated petrophysical evaluation of TMF [27]. TMF was divided into three tiers on the basis of a petrophysical evaluation of the source rock quality: total organic carbon (TOC), porosity, and permeability and hydrocarbon saturation. Tier 1, at the bottom, represents the most organic-rich interval (high maturity) with an average TOC of 7.4% and the best shale characteristics, with high porosity, low clay content, and high hydrocarbon saturation. As illustrated in Figure 3, these excellent properties render Tier 1 the optimal target to place lateral wells. Tier 2 represents intermediate source rock quality with an average TOC of 5.9%, while Tier 3 represents the lowest source rock quality with an average TOC of 3.2%. Isopach maps of the TMF indicate that Tier 3 occupies most of the thickness of the TMF, which is in the range of 110–150 ft TMF, while Tiers 2 and 1 possessed a comparable thickness in the range from 30 to about 40 ft across Jafurah basin [23].

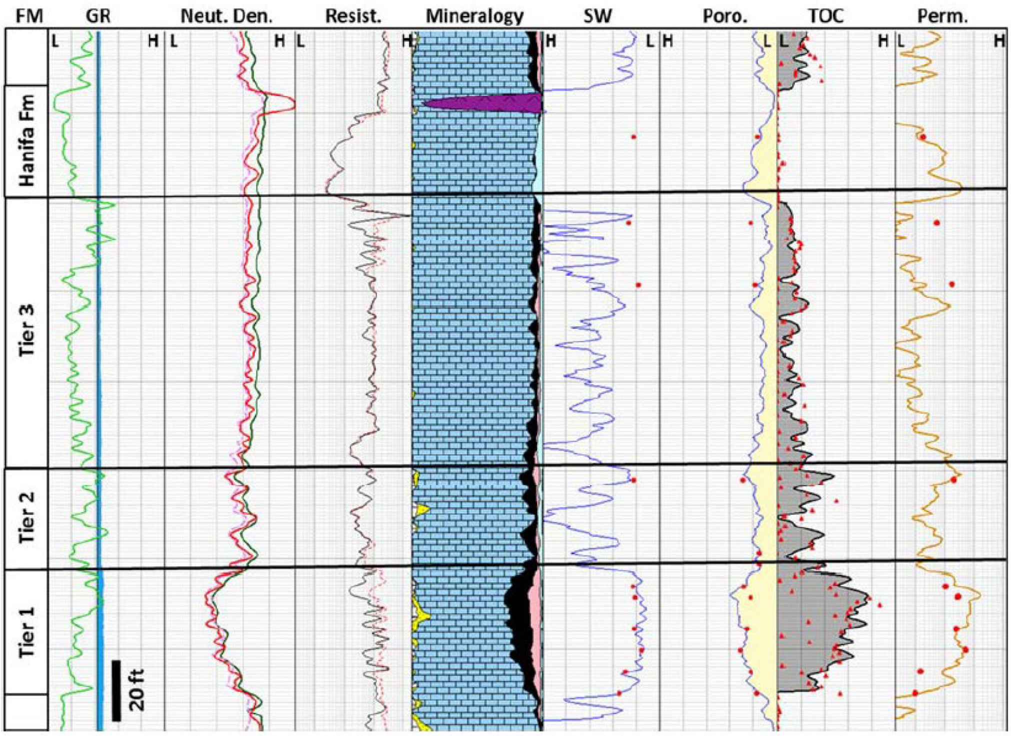

Figure 3. Typical petrophysical model of the Tuwaiq Mountain formation (TMF) in Jafurah basin. The TMF was divided into three units, with Tier 1 exhibiting the best reservoir characteristics. Red dots represent calibration points with available cores [23].

2.3. Mineralogical Composition

X-ray diffraction (XRD) technology was used to identify the rock composition and morphology of TMF. As illustrated in Figure 4, The TMF is mainly composed of organic-rich laminated lime–mud rocks. Calcite is the dominant component with an average of 74% by volume, with a low amount of dolomite, averaging 11% by volume, and a relatively low quartz content, averaging 3% by volume. The total clay content is extremely low, with an average of 5%. The high brittle calcite content and low ductile clay content rendered the TMF the ideal lithology for effective multi-stage hydraulic fracturing [23,27].

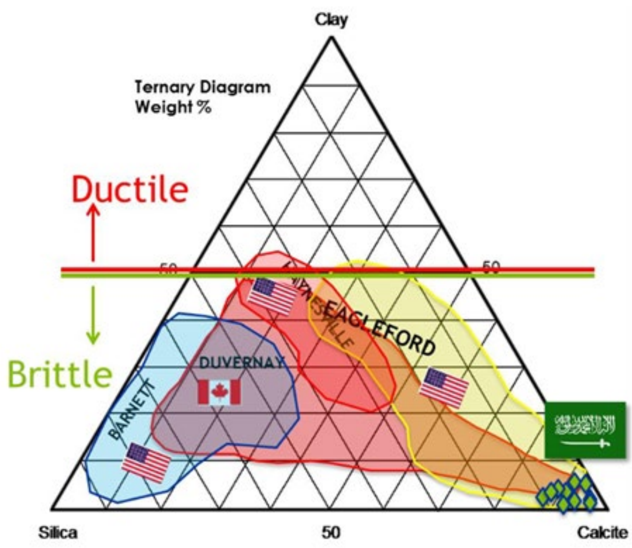

Figure 4. Mineralogical ternary diagram of Tuwaiq Mountain samples (green diamonds) compared with various shale plays [23].

Scanning electron microscopy (SEM) technology was utilized to characterize the pore types of the TMF. As illustrated in Figure 5, the internal texture of the organic matter is mainly composed of nanopores. This type of porosity system is the major pore type in shale gas plays, such as the Eagle Ford. SEM images revealed a well-connected organic pore system in the matrix of the TMF with interconnected porosity averages of around 10%. The pores were mostly irregular polygonal to spherical, with pore sizes of mainly less than 1 μm; the remaining fraction had micropores greater than 1 μm [25,27].

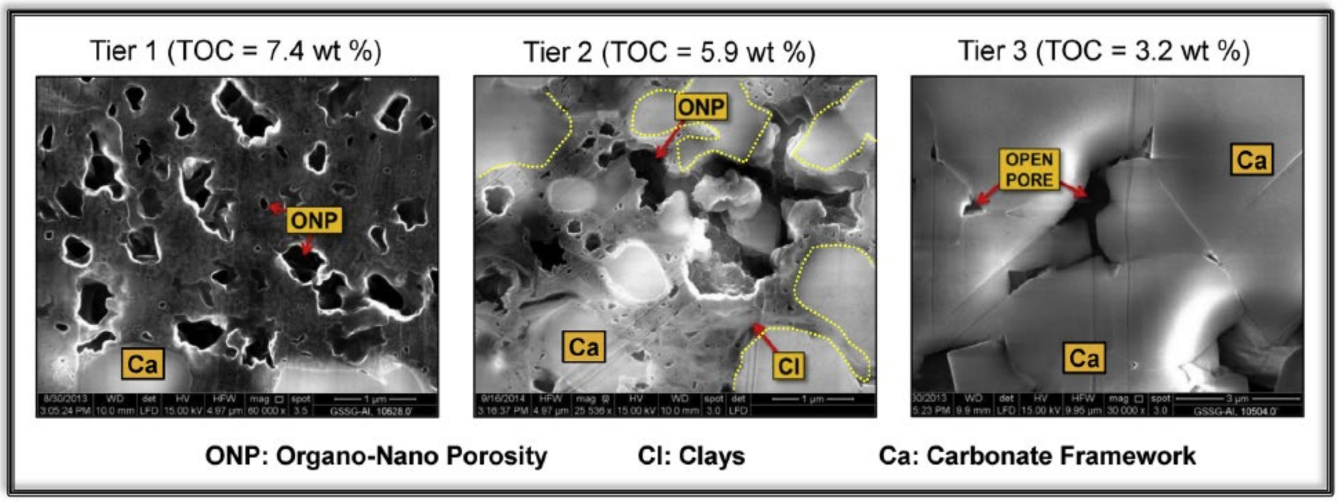

Figure 5. SEM images illustrating the distribution of organic porosity, with Tier 1 showing the highest organic porosity level [27].

2.4. Geomechanics Properties

Understanding geomechanical properties of shale formations is vital for the optimal design of hydraulic fracturing treatments. Experimental studies performed on the elastic and deformational mechanical properties of shale rocks revealed that this type of rock demonstrates a wide range of anisotropic mechanical properties associated with its complicated material composition. Anisotropic mechanical rock tests were completed on representative core samples from Tier 1 of the Tuwaiq Mountain formation [27]. The results show that this zone exhibits a medium level of anisotropy when compared to other highly argillaceous shales. The average static Young's modulus in the horizontal direction (E_h) was 4.81 Mpsi, whereas in the vertical direction (E_v) it was 2.92 Mpsi; hence, the static Young's modulus ratio (E_h/E_v) was about 1.65. The rock exhibited a 0.29 static Poisson's ratio in the horizontal direction (ν_h), and 0.21 in the vertical direction (ν_v); the static anisotropic Poisson ratio (ν_h/ν_v) was about 1.38 [27].

Figure 6 illustrates the influence of soft material (clay and kerogen) content on the static anisotropy E_h/E_v of various shale gas plays [29]. This work shows that the static anisotropy for Young's modulus (E_h/E_v) was directly related to the content of the soft material (clay and kerogen). The measurement for Tier 1 of the Tuwaiq Mountain formation is relatively comparable to that of the Eagle Ford play.

On the basis of diagnostic fractural injectivity tests (DFITs), pore pressure in the TMF was about 0.7 psi/ft at reservoir target depth of 10,000 ft. The local stress regime was characterized by strike–slip conditions, with σ_v = 1.1 psi/ft, σ_{Hmax} = 1.2 psi/ft, and σ_{hmin} = 0.96 psi/ft. The direction of the minimal regional stress was NW, prompting for field development with lateral wells extending in the NW–SE direction [28]. The average elastic properties of the TMF are presented in Table 1 [27].

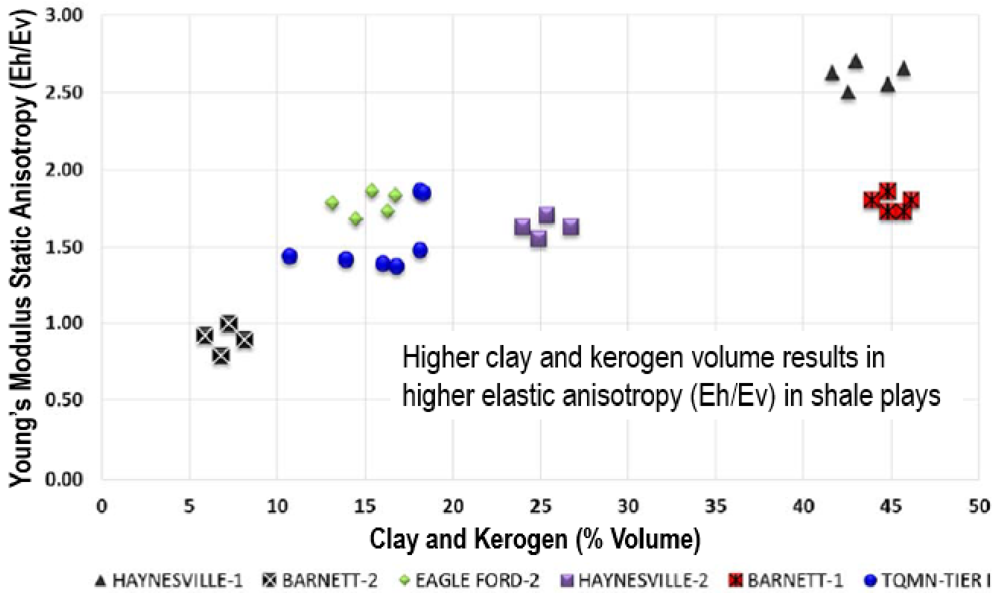

Figure 6. Effect of clay and kerogen content on static anisotropy Eh/Ev. Data for the Tuwaiq Mountain formation are shown in blue [27].

Table 1. Average static Young's modulus and Poisson's ratio.

Average Static Young's Modulus	
Horizontal direction (E_h)	4.81 Mpsi
Vertical direction (E_v)	2.92 Mpsi
Static Young's modulus ratio (E_h/E_v)	1.65
Average Static Poisson's ratio	
Horizontal direction (v_h)	0.29
Vertical direction (v_v)	0.21
Static anisotropic Poisson ratio (ν_h/ν_v) is	1.38

3. Analytical Modeling

3.1. Stress Shadow—Isotropic Model

Li and Guo (2014) presented an analytical model to predict the stress alteration induced by a hydraulic fracture in isotropic formations. The main assumptions behind this model are as follows:

(1) The rock is elastic and homogeneous with constant Young's modulus and Poison's ratio.
(2) The rock volume is infinitely large compared to the fractural width, which is assumed to be constant.
(3) The pressure-propped fracture causes rock stress to increase only in the fracture-opening direction.
(4) Instant stress equilibrium is achieved during fracturing with a constant net pressure.

On the basis of this model, the stress alteration in the direction normal to the fractural surface can be expressed as follows:

$$\Delta\sigma_x = P_{net} e^{\frac{-2P_{net}}{E\ w_f}\ x} \tag{1}$$

The stress alteration along the fractural propagation direction is given by

$$\Delta\sigma_y = \Delta\sigma_x\ \frac{v\ w_f E}{2L_f P_{net}} \tag{2}$$

In above equations, P_{net} is the net pressure (psi), E is the Young's modulus of the rock (psi), v is the Poisson's ratio of the rock (dimensionless), w_f is the fractural width (in), and x is the distance from the fractural surface (ft).

As in normal stress regimes, for wellbore stability purposes, the horizontal wellbore is drilled along the direction of minimal horizontal stress, and fractures are transverse and propagating perpendicular to the least principal stress. Therefore, as depicted schematically in Figure 7, $\Delta\sigma_x = \Delta\sigma_h$ and $\Delta\sigma_y = \Delta\sigma_H$.

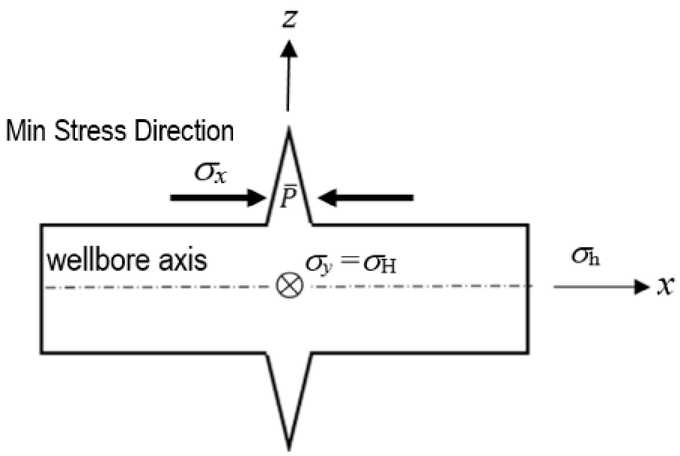

Figure 7. Transverse fracture propagating in a wellbore drilled along the minimal horizontal stress direction.

As represented by the above equations, stress alteration decays exponentially with distance. The decline rate is directly proportional to the net closure pressure, and inversely proportional to the Young's modulus and fractural width.

In isotropic formations, the PKN model [30] is commonly used to calculate the width of a vertically contained fracture (w_{ISO}), with a larger length than height as follows:

$$w_{ISO} = \frac{2h\left(1 - v^2\right)}{E} P_{net} \quad (3)$$

where h is the fractural height (ft).

The new normal principal stresses to the fractural surface and along the fracture-propagation direction can be expressed with the following equations, respectively:

$$\sigma_x = \sigma_h + \Delta\sigma_x \quad (4)$$

$$\sigma_y = \sigma_H + \Delta\sigma_y \quad (5)$$

where σ_h and σ_H are the minimal and maximal horizontal in situ stresses, respectively. The authors in [12] used the input data of Table 2 to predict the stress alteration and new principal stresses.

Table 2. Reservoir and fractural parameters used to predict stress alteration [12].

Parameter	Value
Young's modulus (psi)	7.3×10^6
Fractural half-length (ft)	500
Fractural half-height (ft)	150
Fractural width (in)	0.1575
Net closure pressure (psi)	167
Maximal horizontal stress (psi)	6400
Minimal horizontal stress (psi)	6300
Poisson's ratio	0.20

The results presenting the normalized stress alteration to the net pressure versus the normalized distance from the fracture are shown in Figure 8. As expected, since the fracture propagated perpendicular to the minimal stress direction, the magnitude of the stress alteration along the minimal stress direction was greater than that of the maximal stress direction.

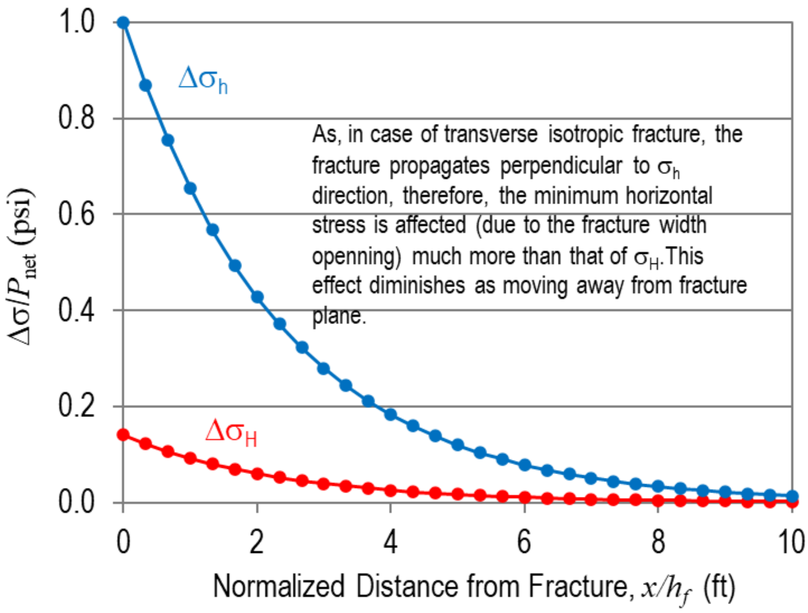

Figure 8. Fracture-induced stress profiles normalized with net pressure as a function of normalized distance from a hydraulic fracture (after [18]).

Figure 9 presents the new principal stresses after the fracture opening as a function of the distance from the fracture. The intersectional point of the two curves represents the point of the isotropic stress condition where $\sigma_h = \sigma_H$, which gives the minimal fractural spacing required to prevent fractural merging. To the left of this point, σ_H, was less than σ_h because of the stress shadow. This point of isotropic stress is mathematically given by:

$$x = -\frac{E_p w_f}{2P_{net}} ln\left[\frac{\sigma_H - \sigma_h}{\left(1 - \frac{w_f E_p \mu}{2L_f P_{net}}\right) P_{net}}\right] \quad (6)$$

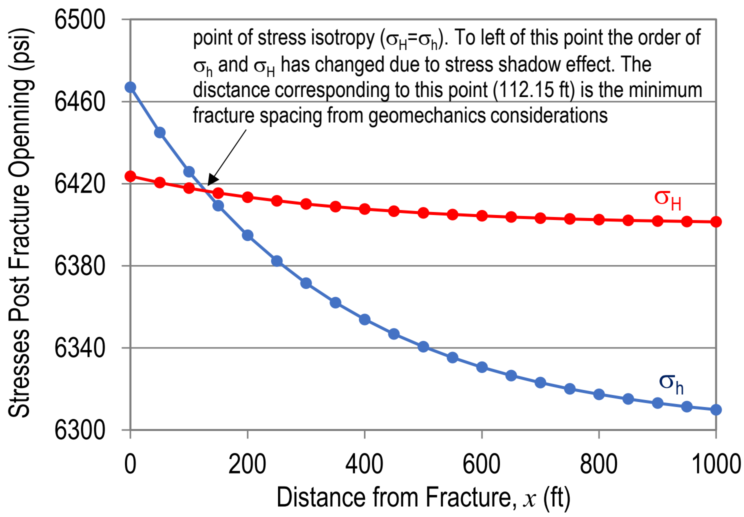

Figure 9. Determination of minimal fractural spacing based on an analytical model (after [18]).

For a positive value of the minimal fractural spacing, it is required that the expression of the natural logarithm be less than 1.0, which implies this condition:

$$P_{net} > \frac{\sigma_H - \sigma_h}{1 - \frac{W_f\ E_P\ \mu}{2L_f\ P_{net}}} \tag{7}$$

As discussed previously, the stress regime in the Jafurah basin and within the TMF reservoir is strike-slip. The order gradient of stresses was σ_H = 1.2 psi/ft > σ_v = 1.1 psi/ft > σ_h = 0.96 psi/ft. At an average reservoir depth of 10,000 ft, the order and magnitude of the stresses were σ_H = 12,000 psi > σ_v = 11,000 psi > σ_h = 9600 psi.

Applying the above stress values, and average Young's modulus of E = 3.8 × 106 psi and Poisson's ratio of v = 0.25 into Equation (7) resulted in minimal net pressure of P_{net} > 2400 psi in order to obtain larger fractural spacing than zero. In a real situation, the net pressure is much less than this. This means that there is no minimal spacing concern from the stress-shadow point of view. Referring to the discussion of the previous subsection, it is evident that the large horizontal stress anisotropy of $\sigma_H - \sigma_h$ = 2400 psi is the reason for this result. In fact, in strike-slip stress regime fields, such as in Jafurah, one of the horizontal stresses exceeds the vertical stress, and this increases the anisotropy of horizontal stresses. This impacts the fractural geometry and, as was shown, reduces the minimal fractural spacing to avoid stress shadows.

Assuming net pressures P_{net} = 250 psi and P_{net} = 1000 psi, the corresponding fractural widths based on Equation (3) were w_{iso} = 0.22 inch and w_{iso} = 0.87 inch, respectively. The stress anisotropy had no effect on fractural width, but the minimal horizontal stress controlled it, as the net pressure was the difference between the fractural pressure and the minimal stress that acted perpendicular to the fractural plane ($P_{net} = P_f - \sigma_h$).

3.2. Stress Shadow—Anisotropic Model

The assumptions in the analytical model of [31,32], which was presented in the preceding section, or any similar models based on a constant-width fracture propagating in a homogeneous isotropic medium with constant values of Young's modulus and Poisson's ratio are not valid for formations with inherent anisotropic properties.

An example of an analytical model to estimate the width of a propagating hydraulic fracture in a TIV medium was presented by [31]. According to this model, the TIV width (w_{TIV}) is calculated as follows:

$$w_{\mathrm{TIV}} = h\sqrt{\frac{1 - v_H^2}{2G_{VH}E_H}}\left(\sqrt{g_1 - h_1} + \sqrt{g_1 + h_1}\right)P_{net} \tag{8}$$

where

$$g_1 = \left(1 - \frac{2G_{VH}}{E_V}(1 + v_H)v_V\right) \tag{9}$$

$$h_1 = \sqrt{1 - \frac{4G_{VH}}{E_V}(1 + v_H)v_V - \frac{4G_{VH}^2}{E_V E_H}(1 + v_H)\left(1 - v_H - 2\frac{E_H}{E_V}v_V^2\right)} \tag{10}$$

In the above equations E_v and E_H are the Young's modulus in the perpendicular and parallel directions with respect to the bedding (psi). Corresponding Poisson's ratios in similar directions are shown as v_v and v_h; G_{vH} is the shear modulus, given by

$$G_{vH} = \frac{E_{45}}{2\ (1 + v_{45})} \tag{11}$$

where E_{45} and v_{45} are the Young's modulus and Poisson's ratios measured on a sample oriented at 45° to the bedding plane.

This analytical approach was adopted in this work to investigate the effect of anisotropic fractural width (w_{TIV}) on stress-shadow development and fractural-spacing determination. Anisotropic fractural width Equation (8) was simplified into Equation (3) for the isotropic case if we replaced $E_v = E_H = E$ and $v_v = v_H = v$, and

$$G_{vH} = G = \frac{E}{2\,(1+v)} \tag{12}$$

The commonly observed characteristic of TIV formations is that Young's modulus in the horizontal direction is higher than the vertical counterpart and can be as high as 3.5 [31,32].

The anisotropic elastic properties of TMF were used to estimate the anisotropic width of a hydraulic fracture. As we did not have the Young' modulus and Poisson's ratio corresponding to samples at 45° with respect to the bedding (E_{45} and v_{45}), to calculate G_{vH} from Equation (12), we used the upscaling approach proposed by to estimate the anisotropic shear moduli. The relationship is expressed as follows:

$$G_{vH} = \frac{E_H}{2(1+v_H)} - \left[1 + \frac{1-v_H}{(1+v_H)(1-2v_H)}\left(\frac{E_H}{E_v} - 1\right)\right]^{-1} \tag{13}$$

This model is based on upscaling a periodically layered material characterized by equal-height layers with different Young's moduli and the same Poisson's ratio [17]. When $\frac{E_H}{E_v} = 1$, i.e., in the case of isotropic formations, Equation (13) converges into Equation (12), as expected. On the basis of Equation (13), G_{vH} = 1.0 × 10^6 psi. Assuming P_{net} = 250 psi and P_{net} = 1000 psi, the corresponding anisotropic fractural widths are w_{TIV} = 0.149 inches and w_{TIV} = 0.770 inches, respectively. Comparing these results with the corresponding isotropic fractural width values in the previous section shows that the anisotropic fractural widths tended to be lower than the isotropic ones. This means that, considering the TIV nature of TMF, similar to other shale formations, fractural width is reduced, which, in turn, requires less fractural spacing. This reduces the concern with regard to the minimal fractural spacing requirements from geomechanical perspective, which facilitates design purposes.

In addition to the effect of the TIV nature of the TMF on fractural width, its impact on the horizontal stresses should also be taken into consideration. This effect additionally impacts fractural width and spacing, as is discussed in the next section.

3.3. In Situ Stresses in Transverse Isotropic Formations

Poroelastic equations are mostly used to calculate the magnitude of horizontal stresses. These equations, assuming isotropic rock properties, are expressed as follows [33]:

$$S_H = \frac{\nu}{1-\nu}\left(S_v - \alpha P_p\right) + \alpha P_p + \frac{E\varepsilon_H}{1-\nu^2} + \frac{\nu E\varepsilon_h}{1-\nu^2} \tag{14}$$

$$S_h = \frac{\nu}{1-\nu}\left(S_v - \alpha P_p\right) + \alpha P_p + \frac{E\varepsilon_h}{1-\nu^2} + \frac{\nu E\varepsilon_H}{1-\nu^2} \tag{15}$$

In the above equations, S_v is the vertical or overburden stress that has a typical gradient of 1 psi/ft, P_p is the pore pressure, α is Biot's coefficient that is usually considered 1.0 for applications in drilling, and ε_H and ε_h are tectonic strains in the directions of maximal and minimal horizontal stresses. These equations basically state that horizontal stresses are a function of vertical stress (first term) affected by pore pressure (second term) and tectonics (third term).

Modified poroelastic Equations (14) and (15) assuming TIV properties for the formation are expressed as follows [34]:

$$S_H = \frac{E_H}{E_v}\frac{\nu_v}{1-\nu_H}\left(S_v - \alpha P_p\right) + \alpha P_p + \frac{E_H\varepsilon_H}{1-v_H^2} + \frac{\nu_H E_H\varepsilon_h}{1-v_H^2} \tag{16}$$

$$S_h = \frac{E_H}{E_v}\frac{\nu_v}{1-\nu_H}\left(S_v - \alpha P_p\right) + \alpha P_p + \frac{E_H \varepsilon_h}{1-\upsilon_H^2} + \frac{\nu_H E_H \varepsilon_H}{1-\upsilon_H^2} \quad (17)$$

The anisotropic coefficient in the above equations is presented as follows:

$$K_{\text{aniso}} = \frac{E_H}{E_v}\frac{\nu_v}{1-\nu_H} \quad (18)$$

In TIV formations, in the horizontal direction (parallel to bedding), the properties are similar but different to those in the vertical direction (perpendicular to the bedding).

If we consider the reported stress gradients for the Jafurah basin ($\sigma_H = 1.2\frac{\text{psi}}{\text{ft}} > \sigma_v = 1.1$ psi/ft $> \sigma_h = 0.96$ psi/ft) correct, inputting these values together with $P_p = 0.7$ psi/ft, an average Young's modulus of $E = 3.8 \times 10^6$ psi, and a Poisson's ratio of $\upsilon = 0.25$ into Equations (14) and (15), we could back calculate the tectonic strains, which are $\varepsilon_H = 0.88$ and $\varepsilon_h = 0.10$. This means that the field is under compressional tectonic stresses that create a strain ratio of $\frac{\varepsilon_H}{\varepsilon_h} = \frac{0.88}{0.10} = \frac{8.8}{1.0}$. This large compressional anisotropy is indeed the reason for the strike-slip stress regime of the field [27,28]. If we now input tectonic strains $\varepsilon_H = 0.88$ and $\varepsilon_h = 0.10$ that we calculated earlier and similar values for the other parameters into Equations (16) and (17), we can calculate the stress gradients with the assumption that the formation is TIV. Thus, we obtain:

$$\sigma_H = 1.37 \text{ psi/ft } > \sigma_v = 1.1 \text{ psi/ft } > \sigma_h = 1.08 \text{ psi/ft} \quad (19)$$

The above results show that the TIV assumption for the formation increases the magnitude of the horizontal stresses. These findings are in a good agreement with in-situ stress results based on anisotropic modeling studies presented in the literature [16,21,34]. In the case of the Jafurah basin, this increase corresponds to σ_H from 1.2 to 1.37 psi/ft and for σ_h is from 0.96 to 1.08 psi/ft.

With the TIV assumption, the minimal horizontal stress gradient becomes very close to the vertical stress gradient, which means that the stress regime in the field becomes very close to the reverse fault regime. In a reverse fault regime, a fracture tends to propagate horizontally, which is not favorable for stimulations in horizontal drilling, as it creates a longitudinal (axial) fracture. Due to a lack of enough data and evidence, it was difficult to confirm this; however, this is something to consider in future stimulation operations, especially if the propagation of twisted fractures is reported.

The anisotropy of horizontal stresses assuming a TIV medium at a depth of 10,000 ft is 13,700 − 10,800 = 2900 psi. This is larger than the 2400 psi for the case of isotropic formation assumption. This means that, with larger horizontal stresses that are expected due to a TIV assumption, there is even less concern about the minimal fractural spacing due to higher stress anisotropy. In addition, due to the larger minimal horizontal stress values, the fractural width was less than that in the isotropic case, which leads to a smaller stress shadow and hence lesser fractural spacing.

In conclusion, ignoring the effect of the TIV nature of shales results in larger fractural width and lesser horizontal stress anisotropy. This means the overestimation of fractural spacing (conservative design), which could lead to ineffective stimulation and production [16,17,31]

4. Effect of Young's Modulus Anisotropy

As discussed in the previous sections, for TIV formations, the horizontal Young's modulus is usually higher than the vertical one. This ratio for Jafurah shale was $\frac{E_H}{E_v} = 1.65$ or $\frac{E_v}{E_H} = 0.61$. Figure 10 shows the changes in fractural width as a function of formation's Young's modulus for TMF data that were calculated using Equations (8)–(10). Here, we set $E_v = 2.92 \times 10^6$ psi, which is the value for TMF, and changed E_H from $E_H = 2.92 \times 10^6$ psi (i.e., the initial minimal horizontal stress value of TMF) to the maximal value of E_H.

The corresponding isotropic width of w_{iso} = 0.1754 inch was calculated on the basis of the assumption of E = 2.92 × 10^6 psi.

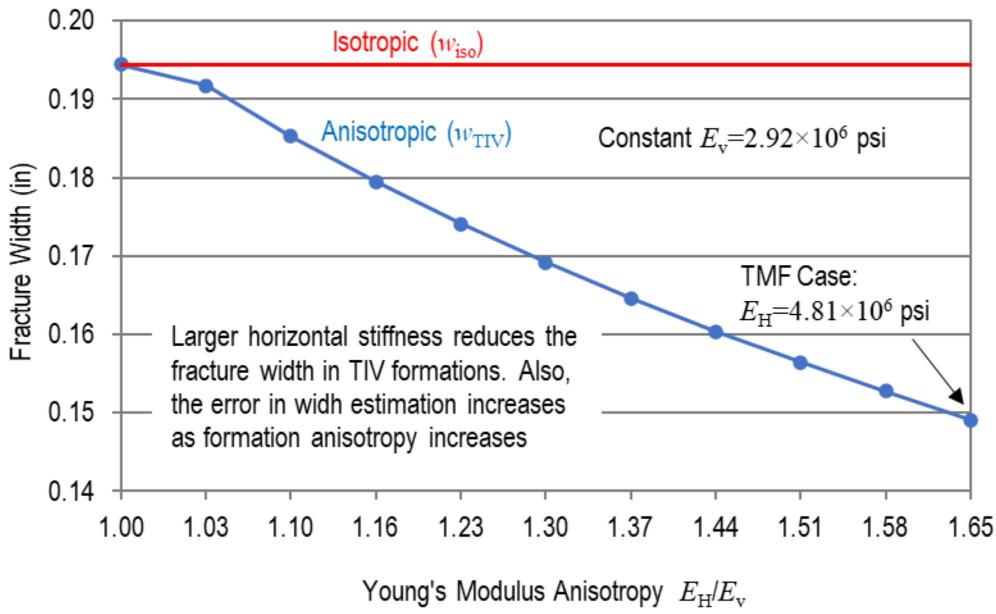

Figure 10. Fractural width changes for TMF as a function of Young's modulus anisotropy.

The results of Figure 10 demonstrate how changing from an isotropic assumption for TMF into an anisotropic ratio of $\frac{E_H}{E_v} = 1.65$ changed the fractural width from 0.1944 to 0.15 inch. Adding to this, the further reduction in fractural width due to the increased minimal horizontal stress value shows the importance of considering the formation anisotropy into the fractural geometry design.

Figure 11 shows the effect of the magnitude of Young's modulus on fractural width, while the Young's modulus anisotropy ratio was constant. Here, we used a TMF stiffness anisotropy ratio of $\frac{E_H}{E_v} = 1.65$ and calculated the change in fractural width as the horizontal Young's modulus was increasing.

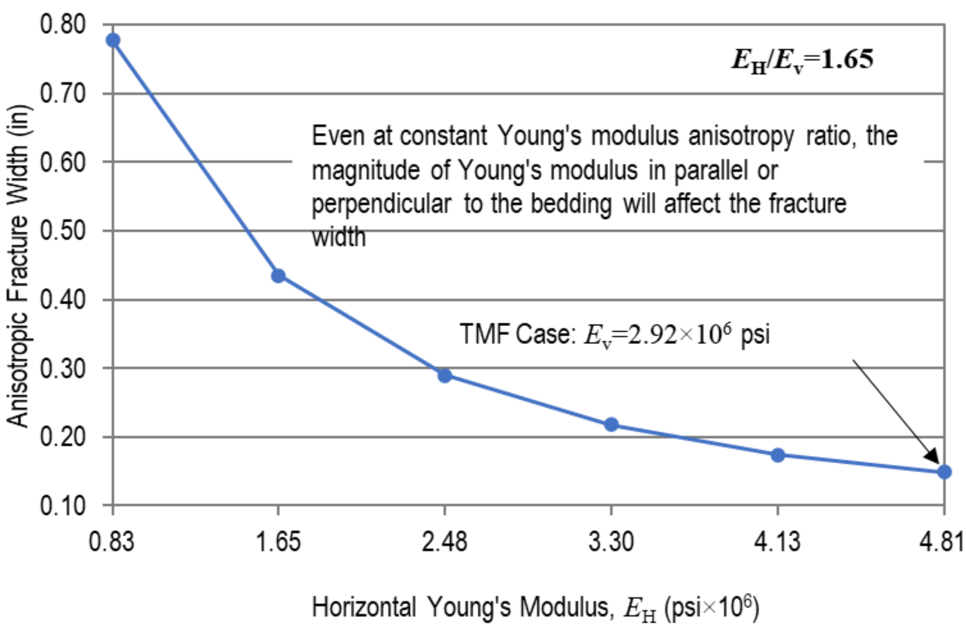

Figure 11. Fractural width changes for TMF as the horizontal Young's modulus changed at a constant Young's modulus anisotropy ratio of $\frac{E_H}{E_v} = \mathbf{1.65}$.

The results show a change in TIV fractural width from 0.78 to 0.15 inch when the horizontal Young's modulus increased from 0.83×10^6 to 4.81×10^6 psi. This was a significant change in fractural width [31,32].

Figure 12 shows the stress shadow calculated for the TMF in directions of the maximal and minimal horizontal stresses. It is evident that the stress disturbance zone around the propagated fracture and the magnitude of stress change were much larger than those of the maximal stress direction. This was because the fracture opened perpendicular to the minimal stress direction, so it had more of an effect along the minimal stress direction. As was expected from Equation (1), the maximal stress change next to the fractural wall in the minimal horizontal stress direction was equivalent to the net pressure, i.e., $\frac{\Delta\sigma_h}{P_{net}} = 1$. Moving away from the fractural wall approximately five times its height, the stresses returned to the original pre-fractural state.

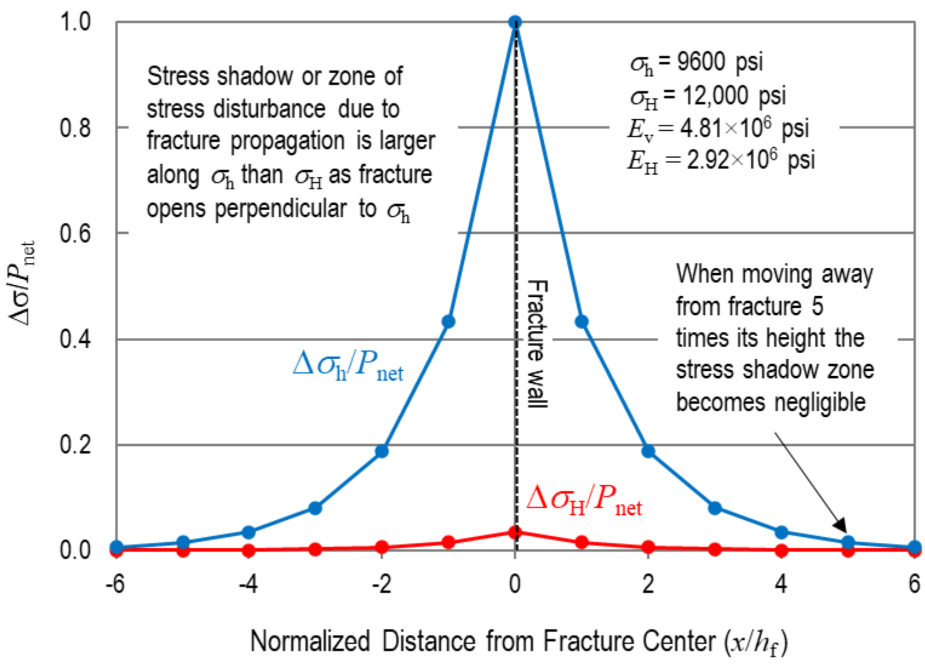

Figure 12. Stress shadow along the minimal and maximal horizontal stress directions in the TMF.

The effect of Young's modulus anisotropy on the stress shadow along the minimal stress direction is plotted in Figure 13. The results show that, in all cases, the stress changes are rapidly reduced as they move away from the fracture and return to the pre-fracture-propagation time at a distance of approximately three to five times the fractural height. However, as the anisotropy ratio increased, the effect of the stress shadow was reduced because the increase in horizontal stiffness reduced the fractural width; thereby, fewer areas around the fracture were affected [21].

The change in Young's modulus anisotropy in this example was from 1 to 5, while its impact on stress-shadow development may not look to be significant. This effect is less when the maximal stiffness anisotropy of TIV formations is generally not expected to exceed 3; in the case of the TMF, it was 1.65. To observe the effect of this amount of stress change on the stress redistribution around the fracture, we plotted the change in the magnitude of σ_h as a function of distance from the fracture. The results of Figure 14 indicate that the fractural propagation had a maximal impact of 250 psi on pre σ_h magnitude, but the stress shadow developed to approximately 400 ft away from the fractural wall before its effect was diminished. This shows that the areas within 100 ft from the fractural wall experience a relatively large changes in stress magnitude [35]. If we consider the stress calculations based on anisotropic poroelastic Equations (16) and (17), stress anisotropy was 2200 psi, which is slightly less than 2400 psi, i.e., the reported values of the stresses that were used in Figure 14, which means that the TIV nature of the TMF may increase the minimal fractural spacing requirements; however, in the case of TMF, it is insignificant.

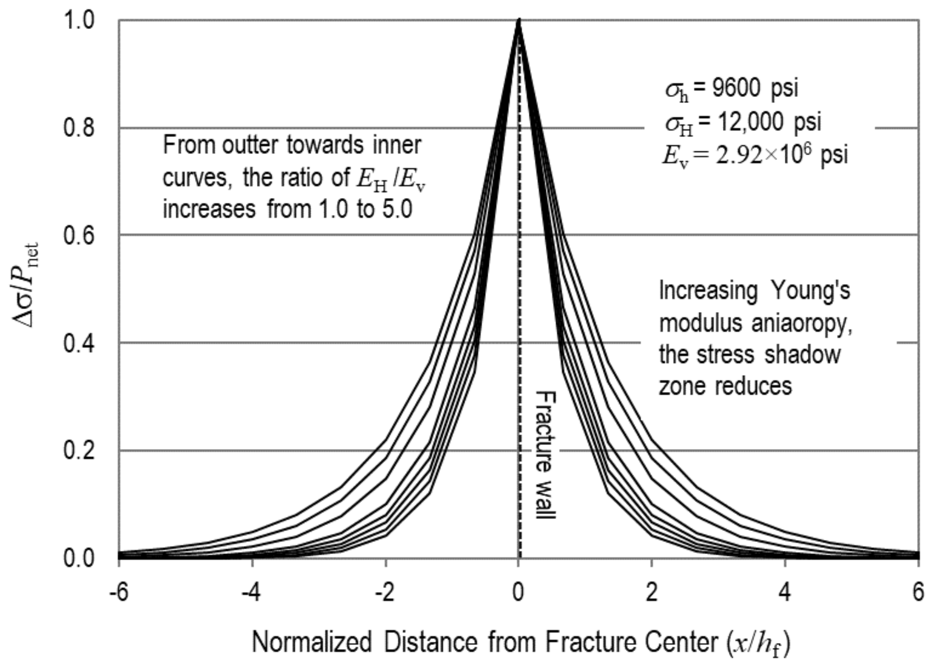

Figure 13. Effect of Young's modulus anisotropy on stress-shadow development along the minimal horizontal stress direction in the TMF.

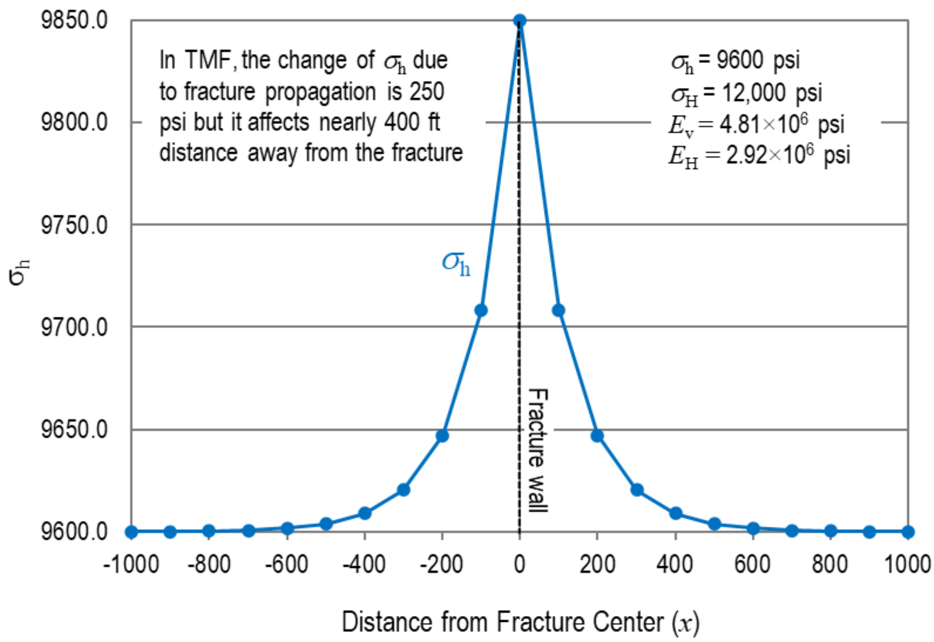

Figure 14. Effect of Young's modulus anisotropy on the change in the minimal horizontal stress magnitude in TMF.

5. Fractural Geometry and Homogenization in TIV Medium

The authors in [17] considered a periodically layered material with two types of layers, characterized by Young's modulus E_i, Poisson's ratio v_i, and thickness h_i. For simplicity, both layers were assumed to have the same thickness and Poisson's ratio (i.e., $h_1 = h_2$ and $v_1 = v_2$). Applying Backus averaging [36], solutions were presented for the elastic constants of the equivalent TIV material, which included horizontal and vertical Young's moduli (E_v and E_H), Poisson's ratios (v_v and v_H) and vertical shear modulus G_{vH}. This approach is also known as homogenization and is depicted in Figure 15.

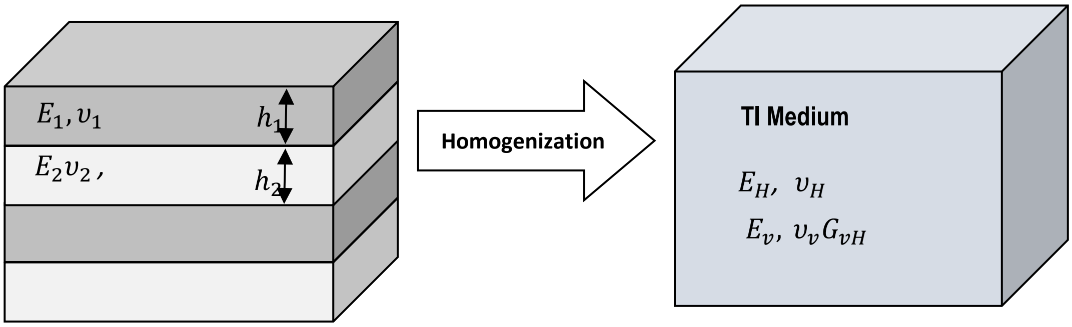

Figure 15. Homogenization concept to represent a periodically layered formation via a homogeneous TI equivalent formation (after [17]).

The components of the stiffness matrix (C), compliance matrix (S), and compliance matrix and TI parameters can be found from the relations presented in Table 3 [17]:

Table 3. Components of the stiffness and compliance matrices, and their relationship with TI parameters [17].

Stiffness Matrix Components (C)	Compliance Matrix Components (C)	TI Parameters
$C_{11} = \frac{1}{(1-v^2)} < E > + \frac{v^2}{(1-v^2)(1-2v)} < E^{-1} >^{-1}$ $C_{12} = \frac{v}{(1-v^2)} < E > + \frac{v^2}{(1-v^2)(1-2v)} < E^{-1} >^{-1}$ $C_{13} = \frac{v}{(1+v)(1-2v)} < E^{-1} >^{-1}$ $C_{33} = \frac{(1-v)}{(1+v)(1-2v)} < E^{-1} >^{-1}$ $C_{44} = \frac{1}{2(1+v)} < E^{-1} >^{-1}$	$S_{11} = \frac{1}{\Delta}\frac{C_{11}-C_{13}^2/C_{33}}{C_{11}-C_{12}}$ $S_{12} = -\frac{1}{\Delta}\frac{C_{12}-C_{13}^2/C_{33}}{C_{11}-C_{12}}$ $S_{13} = -\frac{1}{\Delta}\frac{C_{13}}{C_{33}}$ $S_{33} = \frac{1}{\Delta}\frac{C_{11}+C_{12}}{C_{33}}$ $S_{44} = \frac{1}{C_{44}}$ $\Delta = C_{11} + C_{12} - 2C_{13}^2/C_{33}$	$S_{11} = \frac{1}{E_H}$ $S_{12} = -\frac{v_H}{E_H}$ $S_{13} = -\frac{v_v}{E_v}$ $S_{33} = \frac{1}{E_v}$ $S_{44} = \frac{1}{G_{vH}}$

In the above equations, $< \cdot >$ denotes the average of a quantity over a unit cell of the periodic material. This average was reduced to the mean since the layers had the same thickness.

The Thomsen parameters are commonly used to capture the anisotropy of a TIV medium. These are three non-dimensional combinations that are reduced to zero in isotropic cases and are defined as follows [37]:

$$\varepsilon_T = \frac{C_{11} - C_{33}}{2C_{33}} \tag{20}$$

$$\gamma_T = \frac{C_{66} - C_{44}}{2C_{44}} \tag{21}$$

$$\delta_T = \frac{(C_{13} + C_{44})^2 - (C_{33} - C_{44})^2}{2C_{33}(C_{33} - C_{44})} \tag{22}$$

where parameters ε_T and γ_T show the compressional and shear anisotropy, respectively. Parameter δ_T is more difficult to understand physically, but it is easy to measure, and captures the relationship between the required velocity to flatten gathers (the NMO velocity) and the zero-offset average velocity as recorded with check shots [37]. Alternatively, if the elastic moduli and Poisson's ratios of the TI medium are known, the harmonic average of the Young's modulus, shear moduli, and vertical Poisson's ratio of the TI medium can be found from the relations of Table 4 [17].

Table 4. Elastic moduli and Poisson's ratios of the TI medium [17].

Harmonic average of Young's modulus
$$< E^{-1} >^{-1} = \frac{(1+v_H)(1-2v_H)}{(1-v_H)}\left[\frac{1}{E_v} - \frac{2v_H^2}{(1-v_H)E_H}\right]^{-1}$$
Shear moduli of TI medium
$$G_{vH} = \frac{E_H}{2(1+v_H)} - \left[1 + \frac{1-v_H}{(1+v_H)(1-2v_H)}\left(\frac{E_H}{E_v} - 1\right)\right]^{-1}$$
Vertical Poisson's ratio if $< E >= E_h$ and $v = v_h$
$$v_v = v_h \frac{E_v}{E_H}$$

The aspect ratio of the uniformly pressurized crack can be estimated from the ratio of the apparent compliances of the horizontal and vertical fractural tips [17]:

$$\gamma = \frac{\mathcal{H}_H}{\mathcal{H}_v} \tag{23}$$

$$\mathcal{H}_H = \frac{1}{2\pi}\sqrt{\frac{C_{33}}{C_{11}C_{33} - C_{13}^2}\left(\frac{1}{C_{44}} + \frac{2}{C_{13} + \sqrt{C_{11}C_{33}}}\right)} \tag{24}$$

$$\mathcal{H}_v = \frac{1}{\pi}\frac{C_{11}}{C_{11}^2 - C_{12}^2} \tag{25}$$

The apparent Young's moduli of the crack tip propagating in the horizontal (ϕ = 0) and vertical ($\phi = \pi/2$) directions is presented as follows [17]:

$$E'_0 = \frac{1}{\pi\mathcal{H}_H} \quad E'_{\pi/2} = \frac{1}{\pi\mathcal{H}_v} \tag{26}$$

Hence, the aspect ratio of the uniformly pressurized crack can then be written in terms of these moduli as follows [17].

$$\gamma = \frac{E'_{\pi/2}}{E'_0} \tag{27}$$

6. Fractural Geometry versus Fracture-Propagation Regimes

The propagation of a hydraulic fracture with zero lag is governed by two competing dissipative processes associated with fluid viscosity and solid toughness, and two competing components of the fluid balance associated with fluid storage in the fracture and fluid storage in the surrounding rock (leak-off), as described by Peirce and in [38]. Consequently, limiting propagation regimes can be associated with the dominance of one of the two dissipative processes and/or the dominance of one of the two fluid storage mechanisms. Thus, we could identify four primary asymptotic regimes of hydraulic-fracture propagation (with zero lag) where one of the two dissipative mechanisms and one of the two fluid storage components vanish: storage-viscosity (M), storage-toughness (K), leak-off-viscosity $(\widetilde{M})$, and leak-off-toughness $(\widetilde{K})$-dominated regimes [39]. For example, in the storage-viscosity-dominated regime (M), fluid leak-off is negligible compared to fluid storage in the fracture, and the expended energy in fracturing the rock is negligible compared to viscous dissipation. The solution in the limiting storage-viscosity-dominated regime is given by zero-toughness, zero-leak-off solution $K' = C' = 0$ [39]. The evolution parameters can take the meaning of a toughness $(\mathcal{K}_m, \mathcal{K}_{\widetilde{m}})$, viscosity $(\mathcal{M}_k, \mathcal{M}_{\widetilde{k}})$, storage $(\mathcal{P}_{\widetilde{m}}, \mathcal{P}_{\widetilde{k}})$, or leak-off $(\mathcal{L}_m, \mathcal{L}_k)$ coefficient. These four solution regimes are shown in Figure 16 in a rectangular phase diagram [39].

For each of the four primary regimes of hydraulic-fracture propagation corresponding to the vertices of the diagram, both P_1 and P_2 for that scaling are zero. For example, at the M-vertex, only viscous dissipation takes place, and all the injected fluid is contained in the fracture (so that $\mathcal{K}_m = 0$ and $\mathcal{L}_m = 0$). In a small-scale laboratory test considering the case of a penny-shaped fracture, it is most likely that toughness controls the fracture-propagation regime at the final stage of propagation after a specific period of time. However, almost all the field-scale hydraulic fractures over nearly their entire propagation history are viscosity-dominated [38]. For this purpose, a set of dimensionless groups of physical parameters that describe a specific fracturing process are defined in a way that they become identical using laboratory and field parameters. These dimensionless variables are driven from fluid-flow (mass and momentum conservation laws) and rock-behavior (rock deformation, crack opening and extension) partial differential equations [38]. In this investigation, we used the near-tip asymptotic solutions for the fracture driven by Herschel–Bulkley fluid [17]. The shear stress (τ) for this fluid depends on the shear strain rate ($\dot{\gamma}$) as follows:

$$\tau = \tau_0 + k\dot{\gamma}^n \tag{28}$$

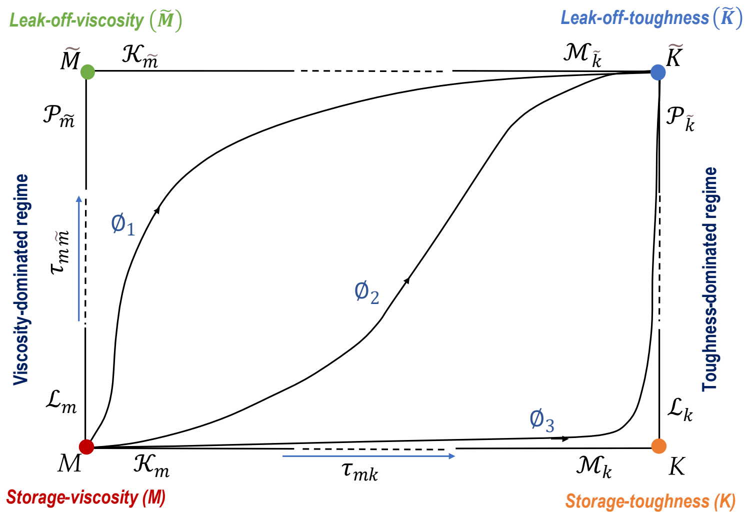

Figure 16. Parametric space diagram for fracture-propagation regimes [39].

Here, τ_0 is yield stress, k is the consistency index, and n is the flow index. When $\tau_0 = 0$ and $n = 1$, they represent a Newtonian fluid with viscosity $k \equiv \mu$. Figure 17 shows the geometry of s vertical elliptical crack with aspect ratio of s vertical to horizontal semi-axis of the crack ($\frac{a}{b}$) in plane xz and width of w_0 in plane yz.

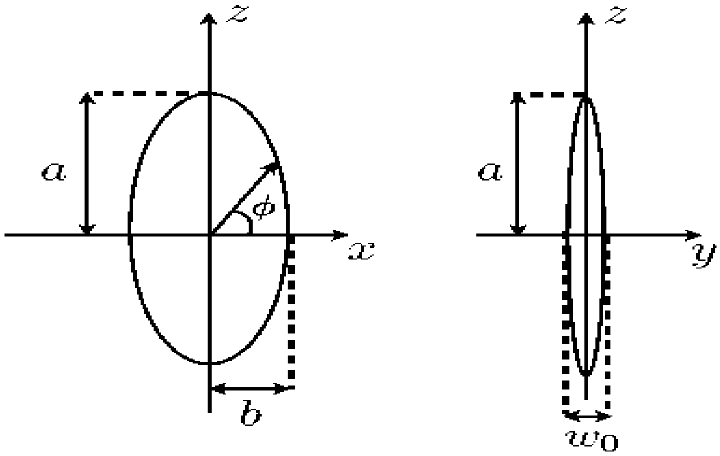

Figure 17. (a,b) Vertical elliptical crack geometry with semi-axes in a TI material [16].

Table 5 presents the summary of the formulations for a fractural aspect ratio and width corresponding to the fractural tip asymptotic solutions related to three fracture-propagation regimes of toughness, viscosity, and τ asymptotes.

Table 5. Fractural aspect ratio and width corresponding to the fracture's near tip asymptotic solutions for different fracture-propagation regimes (after [17]).

Regime.	Fractural Geometry	Comments
Toughness-dominated regime	**Fractural Width** $\omega_k = \sqrt{\frac{32}{\pi}\frac{K_{Ic}}{E'}s^{0.5}}$ $E' = \frac{E}{1-v'}$ **Fractural Aspect Ratio** $\gamma_k = \frac{a}{b} = \left(\frac{K^H_{Ic}}{K^v_{Ic}}\frac{E'_{\pi/2}}{E'_0}\right)^2$	s: distance from the fractural tip. Asymptotic solution is independent of fluid rheology. K_{Ic}: fractural toughness. E_0: plane strain Young's modulus. If $K^v_{Ic} = K^H_{Ic}$, then: $\gamma^K_k = \left(\frac{E'_{\pi/2}}{E'_0}\right)^2$ If fractural energy is direction-independent, i.e., $= \left(\frac{K^v_{Ic}}{E'_{\pi/2}}\right)^2 = \left(\frac{K^H_{Ic}}{E'_0}\right)^2$ then: $\gamma^E_k = \frac{E'_{\pi/2}}{E'_0}$
Viscosity-dominated regime	**Fractural Width** $\omega_{m,n} = \beta_n\left(\frac{M'v^n}{E'}\right)^{\frac{1}{2+n}} s^{\frac{2}{2+n}}$ $\beta_n = \left(\frac{2(2+n)^2}{n}\tan\left(\frac{\pi n}{2+n}\right)\right)^{\frac{1}{2+n}}$ $M' = \frac{2^{n+1}(2n+1)^n}{n^n}k$ **Fractural Aspect Ratio** $\gamma_{m,n} = \left(\frac{E'_{\pi/2}}{E'_0}\right)^{\frac{1}{2+n}}$	v: propagation velocity of the fractural tip. M': scaled consistency index. μ': scaled fluid viscosity. For Newtonian fluid: $M' = \mu' = 12\mu$ and $\beta_n = \beta_{n=1}$ and: $\omega_{m,n=1} = \beta_{n=1}\left(\frac{\mu' v}{E'}\right)^{\frac{1}{3}} s^{\frac{2}{3}}$ for Newtonian fluid: $\gamma_{m,n=1} = \left(\frac{E'_{\pi/2}}{E'_0}\right)^{\frac{1}{3}}$
τ -asymptote	**Fractural Width** $\omega_\tau = 2\sqrt{2\pi}\sqrt{\frac{\tau_0}{E'}}\, s$	**Fractural Aspect Ratio** $\gamma_\tau = \left(\frac{E'_{\pi/2}}{E'_0}\right)^{\frac{1}{2}}$

The equations of Table 5 suggest that the aspect ratio of the elliptical crack for each regime of propagation depended on the different powers of the ratio between the effective plane strain Young's moduli of the horizontal and the vertical fractural tips ($E'_{\pi/2}/E'_0$). The material anisotropy had the most significant influence on the aspect ratio of the crack for the toughness-dominated regime; the largest value occurred when $K^v_{Ic} = K^H_{Ic}$. For the viscosity-dominated and τ-dominated regimes, the influence of anisotropy was smaller. The flow index also did not significantly affect the aspect ratio.

Jafurah TMF Data Analysis

In this subsection, we present the results of analytical TIV modeling using TMF data. Table 6 presents additional data used to investigate the fractural geometry and propagation in the TIV medium.

Table 6. Additional input data used for fractural geometry analysis corresponding to the TMF.

Fluid Rheological Data	**Value**	**Unit**
Yield stress (τ_0)	0.2	Pa
Consistency index (k)	1.0	Pa.s^n
Flow index (n)	0.5	-
Distance from fractural tip (s)	100	ft
Fractural propagation velocity (v)	1000	ft/s
Horizontal fractural toughness ($K^H{}_{IC}$)	27	psi.in$^{0.5}$
Vertical fractural toughness ($K^v{}_{IC}$) psi.in$^{0.5}$	27	psi.in$^{0.5}$

Table 7 shows the calculated values for the components of stiffness and compliance matrices. In Table 8, the Thomsen anisotropic parameters of the TMF are presented. The results show that the shear anisotropy was larger than compressional anisotropy, and that formation generally exhibited anisotropic behavior. Table 9 shows the average elastic properties of the homogenized TI medium. While the Poisson's ratio for the initial layers were considered equivalent (i.e., $v_1 = v_2 = v_H$), the vertical Poisson's ratio for the homogenized TI medium was $v_v = 0.14$.

Table 7. Calculated components of stiffness and compliance matrices corresponding to the TMF.

Stiffness Matrix Components (×10⁶), psi						Compliance Matrix Components (×10⁶), 1/psi					
C_{11}	C_{12}	C_{13}	C_{33}	C_{44}	C_{66}	D	S_{11}	S_{12}	S_{13}	S_{33}	S_{44}
5.93	2.13	1.42	3.47	1.03	1.44	6.90	0.20	−0.06	−0.06	0.34	0.97

Table 8. Thomsen anisotropic parameters corresponding to the TMF.

Compressional anisotropy (ε_T)	0.35
Shear anisotropy (γ_T)	0.42
Short offset effect (δ_T)	0.00

Table 9. Average elastic parameters of homogenized TI medium corresponding to the TMF.

Harmonic average Young's modulus ($<E^{-1}>^{-1}$)	2.65	psi ($\times 10^6$)
Shear modulus (G_{vH})	1.03	psi ($\times 10^6$)
Vertical Poisson's ratio (v_v)	0.14	-

Figure 18 shows the plot of E_H/E_v versus E_1/E_2. This plot is insensitive to the magnitude of the stiffness values but the ratios. Here, the plot was produced with the assumption of $v = 0.29$, which corresponds to the horizontal Poisson's ratio of the TMF. From this figure, the following relationship exists:

$$E_H/E_v = 0.1668\,(E_1/E_2) + 0.789, \tag{29}$$

which shows that, for TMF with $E_H/E_v = 1.65$, the equivalent layered formation had a sequence of formations with a Young's modulus ratio of $E_1/E_2 = 5.20$, which was in large contrast to the elastic mechanical properties.

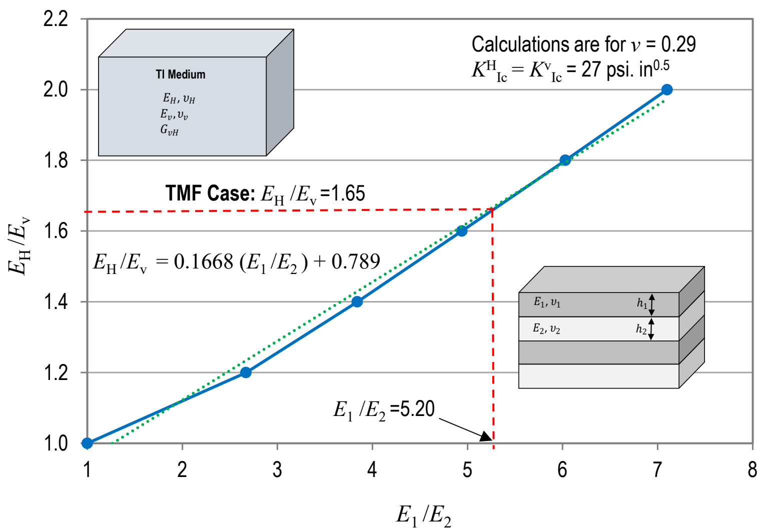

Figure 18. Homogenization concept: TMF TIV formation representation by a layered formation.

Table 10 shows the values of the apparent compliances of the horizontal and the vertical fractural tips ($\mathcal{H}_H$, $\mathcal{H}_v$), apparent Young's moduli of the crack tip propagating in the horizontal and vertical directions (E'_0, $E'_{\pi/2}$), and the fractural aspect ratio. The aspect ratio suggests that, in the absence of any stress containment barrier, and due to the anisotropic nature of TMF, the fracture was 1.28 times greater in length than its height.

Table 10. Apparent compliances of the horizontal and the vertical fractural tips corresponding to the TMF.

Apparent compliance of crack tip propagation in the horizontal direction ($\boldsymbol{\mathcal{H}_H}$)	0.079	1/psi ($\times 10^6$)
Apparent compliance of crack tip propagation in the vertical direction ($\boldsymbol{\mathcal{H}_v}$)	0.062	1/psi ($\times 10^6$)
Apparent Young's moduli of crack tip propagation in the horizontal direction ($\boldsymbol{E'_0}$)	4.04	psi ($\times 10^6$)
Apparent Young's moduli of crack tip propagation in the vertical direction ($\boldsymbol{E'_{\pi/2}}$)	5.16	psi ($\times 10^6$)
Aspect ratio of uniformly pressurized crack ($\delta = \frac{\mathcal{H}_H}{\mathcal{H}_v} = \frac{E'_{\pi/2}}{E'_0}$)	1.28	-

Following the homogenization concept, Figure 19 shows the ratio of the apparent Young's moduli of crack-tip propagation in the vertical to the horizontal directions as a function of the Young's moduli ratio of the original layered formation. In this plot, $v = 0.29$ corresponds to the horizontal Poisson's ratio of the TMF. The following correlation can be established from this plot:

$$E'_{\pi/2}/E'_0 = 0.1668\,(E_1/E_2) + 0.789 \tag{30}$$

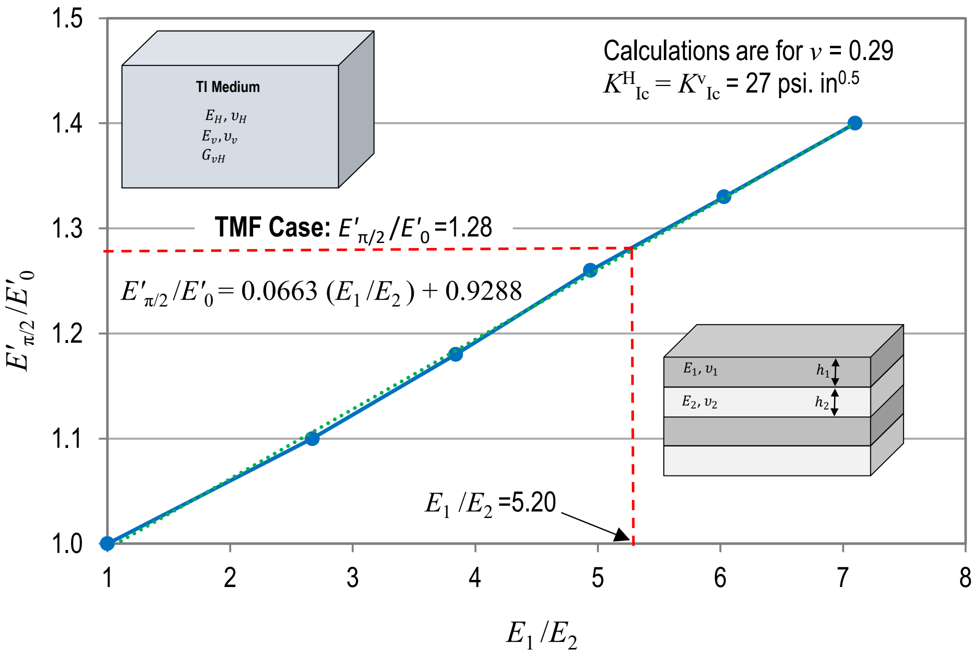

Figure 19. Ratio of the effective Young's moduli of the vertical and horizontal fractural tips as a function of the ratio of Young's moduli of the original layered medium.

From this correlation, the aspect ratio corresponding to TMF ($E_1/E_2 = 5.20$) was calculated: $\gamma = E'_{\pi/2}/E'_0 = 1.28$, which is equal to the value in Table 10.

Table 11 lists the fractural aspect ratios for the TMF assuming different propagation regimes. The elastic anisotropy of the formation had the greatest impact in the case of the toughness-dominated regime, while in the field situations, fracture propagation was primarily viscosity-dominated. In the latter case, the results of Table 11 show that the change in fluid power index from n = 0.5 to n = 1.0 did not have a noticeable change in the fractural aspect ratio (it was reduced from 1.14 to 1.12).

To investigate the effect of the toughness anisotropy on the fractural aspect ratio, we considered the case of the toughness-dominated regime and plotted the results in Figure 20. The results show how the fractural aspect ratio increased as the toughness anisotropy grew. Figure 21 shows the results of the fractural aspect ratio anisotropy for different fracture-propagation regimes. The results, as discussed earlier, show that the maximal anisotropy corresponds to the toughness-dominated regime and then the viscosity-dominated regime. A change in fluid power index (n) also did not show noticeable changes in the fractural aspect ratio, and the t-dominated regime had the lowest width.

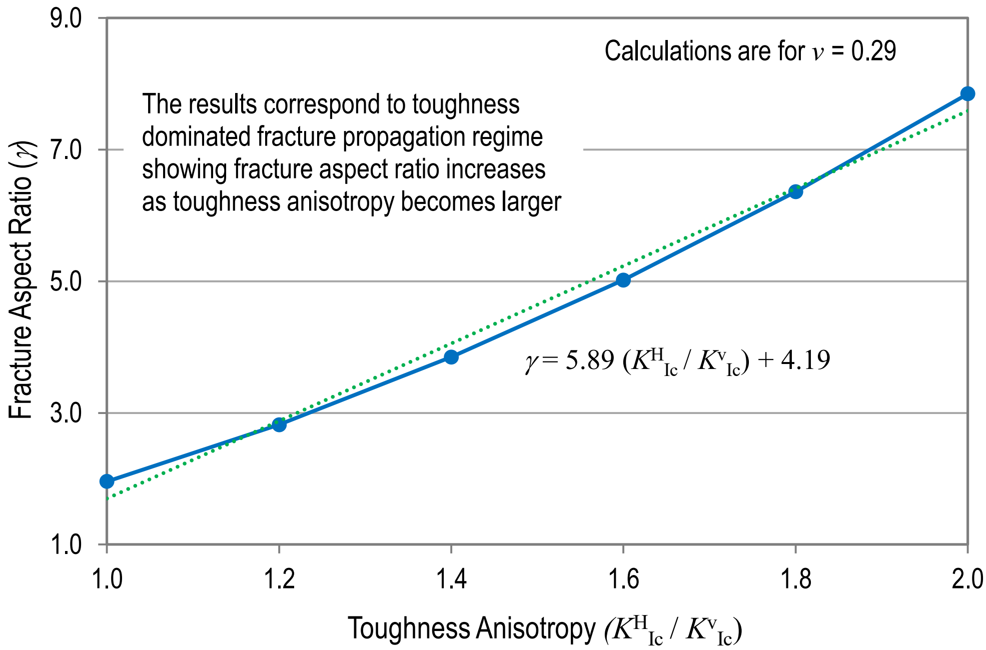

Figure 20. Fractural aspect ratio changes as a function of the formation's toughness in the toughness-dominated propagation regime. Data correspond to the TMF.

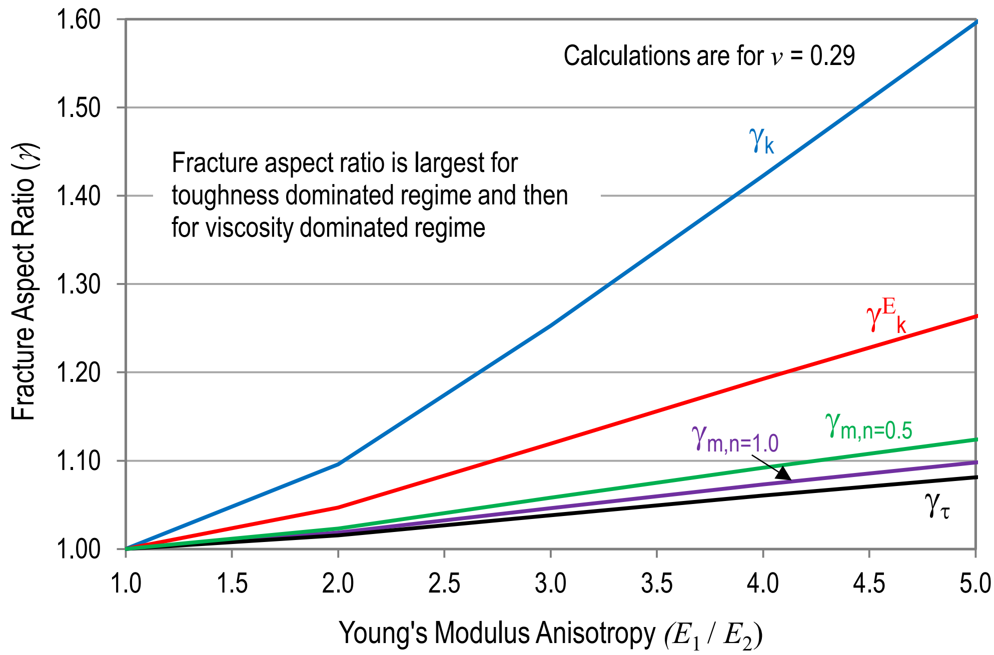

Figure 21. Fractural aspect ratio corresponding to different propagation regimes as a function of the stiffness anisotropy ratio.

Table 11. Fractural aspect ratio corresponding to tip asymptote solutions for different propagation regimes. Data correspond to the TMF.

Propagation Regime	Fracture Aspect Ratio (γ)
Toughness-dominated	1.63
Isotropic fracture energy	1.28
Viscosity-dominated	
$n = 0.5$	1.10
$n = 1.0$	1.08
τ-dominated	1.13

7. Discussion

The above results provide valuable information regarding the fractural geometry corresponding to different propagation regimes. As mentioned before, lab-scale simulations may be more representative in toughness-dominated regimes, whereas in field applications, the viscosity-dominated regime is dominant [17,40]. In real field applications, in the early time of fracturing the propagation regime, toughness dominates, and as time progresses, this changes into a viscosity regime. Hence, a change in the fractural geometry is likely to happen, and these analytical models provide an initial tool to understand fractural aspect ratio changes [40]. The results may be calibrated with micro-seismic data where available.

While TIV analytical models such as the one in [31] provide useful insights into the behavior of hydraulic fractures in anisotropic formations, there are several potential limitations and criticisms of the proposed solution. One potential limitation of the analytical solution is that it assumes a simplified fractural geometry and a homogeneous reservoir. This assumption may not be valid in many shale gas reservoirs where elastic properties can vary significantly due to the presence of natural fractures, heterogeneity, and layering. Neglecting these variations can lead to inaccurate predictions of fractural behavior and width. In addition, the analytical solution assumes that fractures are penny-shaped cracks, which is a simplified representation of the actual fractural geometry. While this assumption may be valid for very small fractures, larger fractures can have complex shapes and non-uniform width distributions. Neglecting these complexities can also result in inaccurate predictions of fractural behavior. Lastly, the analytical solution assumes that the fluid pressure inside a fracture is constant, which may not be the case in real-world scenarios where fluid leak-off, fractural closure, and non-uniform proppant distribution can lead to significant variations in the fluid pressure distribution inside the fracture. Hence, analytical methods are simplified models that rely on assumptions and idealizations. While they can provide useful insights, they should be used in conjunction with more detailed numerical simulations and field data to verify the accuracy of the predictions and optimize fractural spacing in actual shale reservoirs.

8. Conclusions

Analytical modeling was employed in this study to estimate fractural geometry and stresses in an anisotropic medium. The results showed that the Young's modulus anisotropy had a noticeable impact on fractural width, whereas the impact of the Poisson's ratio was minimal. The effect of the stress anisotropy and other rock properties on stress shadows was also investigated. In the presence of a large stress anisotropy, the fractures could be placed close to each other; theoretically, there is no concern regarding minimal fractural spacing. The fractural aspect ratio was estimated in different propagation regimes, and the largest occurred in the toughness-dominated regime.

A comparison of the results for the TMF and Eagle Ford showed that the dominant stress regime in Eagle Ford was normal, whereas it was a strike-slip regime in the TMF. Stress anisotropy was also larger in the TMF, which means less concern in terms of minimal fractural spacing compared to for Eagle Ford. The results of a comparison of the elastic properties also confirmed larger anisotropic properties for TMF than those for Eagle Ford.

Its implications in field operations should be considered in terms of fractural geometry and proppant placements.

Author Contributions: Conceptualization, A.S., methodology, A.S., validation, A.S., investigation, A.S. and A.D., resources, V.R., data curation, A.S. and V.R., writing—original draft preparation, A.S., writing—review and editing, A.S., A.D. and V.R., supervision, V.R. All authors have read and agreed to the published version of the manuscript.

Funding: This research received no external funding.

Data Availability Statement: Data is available upon request.

Acknowledgments: The first Author acknowledges the financial support of the Saudi Aramco Oil Company.

Conflicts of Interest: The authors declare no conflict of interest.

References

1. Muther, T.; Qureshi, H.A.; Syed, F.I.; Aziz, H.; Siyal, A.; Dahaghi, A.K.; Negahban, S. Unconventional hydrocarbon resources: Geological statistics, petrophysical characterization, and field development strategies. *J. Pet. Explor. Prod. Technol.* **2022**, *12*, 1463–1488. [CrossRef]
2. Kapustin, N.O.; Grushevenko, D.A. Global prospects of unconventional oil in the turbulent market: A long term outlook to 2040. *Oil Gas Sci. Technol.* **2018**, *73*, 67. [CrossRef]
3. Yznaga, R.J.A.; Quintero, L.F.; Negm, E.; van Laer, P. Phenomenology during flowback in unconventional wells. In Proceedings of the SPE Middle East Oil and Gas Show and Conference, MEOS, Manama, Bahrain, 18–21 March 2019. [CrossRef]
4. Brandes, C.; Tanner, D.C. Chapter 2—Fault Mechanics and Earthquakes. In *Understanding Faults Detecting, Dating, and Modeling*; Elsevier: Amsterdam, The Netherlands, 2020; pp. 11–80. ISBN 9780128159859. [CrossRef]
5. Bons, P.; Cao, D.; Riese, T.; Esvertit, E.; Koehn, D.; Naaman, I.; Sachua, T.; Rivas, E. A review of natural hydrofractures in rocks. In *Geological Magazine*; Cambridge University Press: Cambridge, UK, 2022. [CrossRef]
6. Bagdeli, M.; Manshad, A.; Shadizadeh, S.; Ali, J.; Gholami, R.; Keshavarz, A.; Iglauer, S. Natural fracture characterization and wellbore stability analysis of a highly fractured southwestern Iranian oilfield. *Int. J. Rock Mech. Min. Sci.* **2019**, *123*, 104101. [CrossRef]
7. Chen, B.; Barboza, B.; Sun, Y.; Bai, J.; Thomas, H.; Dutko, M.; Cottrell, M.; Li, C. A Review of Hydraulic Fracturing Simulation. *Arch. Comput. Methods Eng.* **2021**, *29*, 1–58. [CrossRef]
8. Wang, D.; Dong, Y.; Sun, D.; Yu, B. A three-dimensional numerical study of hydraulic fracturing with degradable diverting materials via CZM-based FEM. *Eng. Fract. Mech.* **2020**, *237*, 107251. [CrossRef]
9. Merzoug, A.; Ellafi, A. Optimization of Child Well Hydraulic Fracturing Design: A Bakken Case Study. In Proceedings of the SPE Oklahoma City Oil and Gas Symposium, Oklahoma City, OK, USA, 17–19 April 2023. [CrossRef]
10. Merzoug, A.; Rasouli, V. Offset Well Design Optimization Using a Surrogate Model and Metaheuristic Algorithms: A Bakken Case Study. *Eng* **2023**, *4*, 1290–1305. [CrossRef]
11. Holditch, S.A. Tight Gas Sands. *J. Pet. Technol.* **2006**, *58*, 86–93. [CrossRef]
12. Roussel, N.P.; Sharma, M.M. Optimizing fracture spacing and sequencing in horizontal-well fracturing. *SPE Prod. Oper.* **2011**, *26*, 173–184. [CrossRef]
13. Wang, X.; Zhang, F.; Tang, M.; Du, X.; Tang, J. Effect of Stress Shadow Caused by Multistage Fracturing from Multiple Well Pads on Fracture Initiation and Near-Wellbore Propagation from Infill Wells. *SPE J.* **2022**, *27*, 204–225. [CrossRef]
14. SPE 151980 Fracture Shadowing: A Direct Method for Determining of the Reach and Propagation Pattern of Hydraulic Fractures in Horizontal Wells. 2012. Available online: http://onepetro.org/SPEHFTC/proceedings-pdf/12HFTC/All-12HFTC/SPE-151980-mokhthe=omMS/1631934/spe-151980-ms.pdf/1 (accessed on 1 March 2023).
15. Patterson, R.A. Characterizing Complex Fracture Geometry through Data Integration in the Permian Basin. Master's Thesis, Texas A&M University, College Station, TX, USA, 2017.
16. Mokhtari, M. SPE-170707-MS Acoustical and Geomechanical Characterization of Eagle Ford Shale-Anisotropy, Heterogeneity and Measurement Scale. 2014. Available online: http://onepetro.org/SPEATCE/proceedings-pdf/14ATCE/All-14ATCE/SPE-170707-MS/1494685/spe-170707-ms.pdf/1 (accessed on 22 April 2023).
17. Bessmertnykh, A.O.; Dontsov, E.V. Title Aspect Ratio of Hydraulic Fracture in Homogeneous Transversely Isotropic Material. 2018. Available online: www.armasymposium.org (accessed on 16 April 2023).
18. Liu, X.; Rasouli, V.; Guo, T.; Qu, Z.; Sun, Y.; Damjanac, B. Numerical simulation of stress shadow in multiple cluster hydraulic fracturing in horizontal wells based on lattice modelling. *Eng. Fract. Mech.* **2020**, *238*, 107278. [CrossRef]
19. Amadei, B. Rock Anisotropy and the Theory of Stress Measurements. In *Lecture Notes in Engineering*; Springer: Berlin/Heidelberg, Germany, 1983; Volume 2. [CrossRef]

20. Khan, S.; Williams, R.E.; Ansari, S.; Khosravi, N. Impact of Mechanical Anisotropy on Design of Hydraulic Fracturing in Shales. In Proceedings of the Abu Dhabi International Petroleum Conference and Exhibition. Society of Petroleum Engineers, Abu Dhabi, United Arab Emirates, 11–14 November 2012; p. 7. [CrossRef]
21. Suarez-Rivera, R.; Green, S.; Mclennan, J.; Bai, M. Effect of Layered Heterogeneity on Fracture Initiation in Tight Gas Shales. In Proceedings of the SPE Annual Technical Conference and Exhibition, San Antonio, TX, USA, 24–27 September 2006; Volume 7. [CrossRef]
22. Zhang, Y.; Liu, H.; Li, Y.; Li, W. Elastic anisotropy controls hydraulic fracture geometry in shale reservoirs. *J. Geophys. Res. Solid Earth* **2021**, *126*, e2020JB020284. [CrossRef]
23. Almubarak, A.; Aramco, S.; Arabia, S.; Hakami, A. Saudi Arabia's Unconventional Program in the Jafurah Basin: Transforming an Idea to Reality with the Jurassic Tuwaiq Mountain Formation. 2017. Available online: http://onepetro.org/WPCONGRESS/proceedings-pdf/WPC22/2-WPC22/D023S002R002/1254732/wpc-22-1223.pdf/1 (accessed on 11 April 2023).
24. Al-Sulami, G.; Boudjatit, M.; Al-Duhailan, M.; Di Simone, S. The unconventional shale reservoirs of jafurah basin: An integrated petrophysical evaluation using cores and advanced well logs. In Proceedings of the SPE Middle East Oil and Gas Show and Conference, MEOS, Manama, Bahrain, 6–9 March 2017; pp. 2874–2884. [CrossRef]
25. Weijermars, R.; Jin, M.; Khamidy, N.I. Workflow for probabilistic resource estimation: Jafurah basin case study (saudi arabia). *Energies* **2021**, *14*, 8036. [CrossRef]
26. Jin, M.; Weijermars, R. Economic appraisal of an unconventional condensate play based on public pilot data prior to field development: Jafurah Basin case study (Saudi Arabia). *J. Nat. Gas Sci. Eng.* **2022**, *103*, 104605. [CrossRef]
27. Hakami, A.; Al-Mubarak, A.; Al-Ramadan, K.; Kurison, C.; Leyva, I. Characterization of carbonate mudrocks of the Jurassic Tuwaiq Mountain Formation, Jafurah basin, Saudi Arabia: Implications for unconventional reservoir potential evaluation. *J. Nat. Gas Sci. Eng.* **2016**, *33*, 1149–1168. [CrossRef]
28. Kurison, C.; Kuleli, H.S.; Mubarak, A.H.; Al-Sultan, A.; Shehri, S.J. Reducing uncertainty in unconventional reservoir hydraulic fracture modeling: A case study in Saudi Arabia. *J. Nat. Gas Sci. Eng.* **2019**, *71*, 102948. [CrossRef]
29. Snee, J.; Zoback, M. State of Stress in Area of Active Unconventional Oil and Gas Develoent in North America. *AAPG Bull.* **2022**, *106*, 355–385. [CrossRef]
30. Perkins, T.K.; Kern, R. Widths of Hydraulic Fractures ABSTRACT. 1961. Available online: http://onepetro.org/JPT/article-pdf/13/09/937/2214269/spe-89-pa.pdf (accessed on 13 March 2023).
31. Chertov, M. Closed-form solution for vertical fracture width in anisotropic elastic formations. *Int. J. Rock Mech. Min. Sci.* **2012**, *53*, 70–75. [CrossRef]
32. Gokaraju, D. Impact of fracture spacing and mechanical parameter anisotropy on fracture width in horizontal wells in shales. 2014. Available online: https://scholarsmine.mst.edu/masters_theses/7253 (accessed on 23 January 2023).
33. Rasouli, V.; Rasouli, F.; Rasouli, P.; Rasouli, V. The effect of horizontal stresses on the stability of vertical and inclined boreholes. *J. Rock Mech. Geotech. Eng.* **2011**, *3*, 2370–2386.
34. Higgins, S.; Goodwin, S.; Donald, A.; Bratton, T.; Tracy, G. SPE 115736 Anisotropic Stress Models Improve Completion Design in the Baxter Shale. 2008. Available online: http://onepetro.org/SPEATCE/proceedings-pdf/08ATCE/All-08ATCE/SPE-115736-MS/2734492/spe-115736-ms.pdf/1 (accessed on 8 January 2023).
35. Zandy, A. Modling and Simulations of Stress Shadow Effect on Multi Stage Hydraulic Fractures. Ph.D. Thesis, University of North Dakota, Grand Forks, ND, USA, 2022.
36. Backus, G.E. Long-wave elastic anisotropy produced by horizontal layering. *J. Geophys. Res.* **1962**, *67*, 4427–4440. [CrossRef]
37. Thomsen, L. Weak elastic anisotropy. *Geophysics* **1986**, *51*, 1954–1966. [CrossRef]
38. Detournay, E. Initiation and propagation of hydraulic fractures in impermeable rocks. *J. Geophys. Res. Solid Earth* **2004**, *4*, 113–125.
39. Peirce, A.; Detournay, E. Fracture propagation regimes: A new interpretation of hydraulic fracture geometry. *J. Pet. Sci. Eng.* **2008**, *6*, 75–93.
40. Benouada, N. Fracture Initiation and Propagations in Shale Formations With Anisotropic Toughness. Ph.D. Thesis, University of North Dakota, Grand Forks, ND, USA, 2022.